Three-dimensional retinal and choroidal capillary imaging by power Doppler optical coherence angiography with adaptive optics

Kazuhiro Kurokawa, Kazuhiro Sasaki, Shuichi Makita, Young-Joo Hong, and Yoshiaki Yasuno[*]

Computational Optics Group, University of Tsukuba, Tsukuba, Japan

[*]*yasuno@optlab2.bk.tsukuba.ac.jp*

http://optics.bk.tsukuba.ac.jp/COG/

Abstract: Retinal and choroidal vascular imaging is a key to the better understanding and diagnosis of eye diseases. To achieve comprehensive three-dimensional capillary imaging, we used an enhanced vascular imaging technique, so called adaptive optics optical coherence angiography (AO-OCA). AO-OCA enables *in vivo* high-resolution and high-contrast micro-vascular imaging by detecting Doppler frequency shifts. Using this technique, the retinal and choroidal vasculatures of healthy subjects were imaged. The results show that both intensity and Doppler power images have sufficient contrast to discriminate almost all vasculatures from the static tissue. However, the choriocapillaris, pre-arterioles, and post-venules in the Sattler layer were more contrasted by the Doppler technique. In conclusion, AO-OCA enables three-dimensional capillary imaging, and is especially useful for the detection of the choriocapillaris and choroidal capillary network.

OCIS codes: (170.4500) Optical coherence tomography; (110.1080) Active or adaptive optics; (170.4470) Ophthalmology; (170.3340) Laser Doppler velocimetry.

References and links

1. Albert Alm, "Circulation," in *Adler's Physiology of the Eye,* P. L. Kaufman and A. Alm, eds. (Mosby, 2002), pp.747–784.
2. J. Flammer, S. Orgül, V. P Costa, N. Orzalesi, G. K. Krieglstein, L. M. Serra, J. P. Renard, and E. Stefánsson, "The impact of ocular blood flow in glaucoma," Prog. Retin. Eye Res. **21**(4), 359–393 (2002), http://www.sciencedirect.com/science/article/pii/S1350946202000083.
3. M. A. Zarbin, "Current concepts in the pathogenesis of age-related macular degeneration," Archives of Ophthalmology **122**(4), 598–614 (2004), http://www.ncbi.nlm.nih.gov/pubmed/15078679.
4. C. J. Pournaras, E. Rungger-Brändle, C. E. Riva, S. H. Hardarson, and E. Stefansson, "Regulation of retinal blood flow in health and disease," Prog. Retin. Eye. Res. **27**(3), 284–330 (2008), http://www.sciencedirect.com/science/article/pii/S135094620800013X.
5. R. F. Gariano and T. W. Gardner, "Retinal angiogenesis in development and disease," Nature **438**(7070), 960–966 (2005), http://www.nature.com/nature/journal/v438/n7070/full/nature04482.html.
6. L. A. Yannuzzi, K. T. Rohrer, L. J. Tindel, R. S. Sobel, M. A. Costanza, W. Shields, and E. Zang, "Fluorescein angiography complication survey," Ophthalmology **93**(5), 611–617 (1986), http://www.ncbi.nlm.nih.gov/pubmed/3523356.

7. M. Hope-Ross, L. A. Yannuzzi, E. S. Gragoudas, D. R. Guyer, J. S. Slakter, J. A. Sorenson, S. Krupsky, D. A. Orlock, and C. A. Puliafito, "Adverse reactions due to indocyanine green," Ophthalmology **101**(3), 529–533 (1994), http://www.ncbi.nlm.nih.gov/pubmed/8127574.

8. D. A. Nelson, S. Krupsky, A. Pollack, E. Aloni, M. Belkin, I. Vanzetta, M. Rosner, and A. Grinvald, "Special report: noninvasive multi-parameter functional optical imaging of the eye," Ophthalmic Surg. Lasers Imaging **36**(1), 57–66 (2005).

9. A. Roorda, F. Romero-Borja, W. Donnelly III, H. Queener, T. J. Hebert, and M. C. W. Campbell, "Adaptive optics scanning laser ophthalmoscopy," Opt. Express **10**(9), 405–412 (2002).

10. J. A. Martin and A. Roorda, "Direct and noninvasive assessment of parafoveal capillary leukocyte velocity," Ophthalmology **112**(12), 2219–2224 (2005), http://www.sciencedirect.com/science/article/pii/S0161642005009115.

11. Z. Zhong, B. L. Petrig, X. Qi, and S. A. Burns, "In vivo measurement of erythrocyte velocity and retinal blood flow using adaptive optics scanning laser ophthalmoscopy," Opt. Express **16**(17), 12746–12756 (2008).

12. J. Tam, J. A. Martin, and A. Roorda, "Noninvasive visualization and analysis of parafoveal capillaries in humans," Invest. Ophthalmol. Vis. Sci. **51**(3), 1691–1698 (2010), http://www.iovs.org/content/51/3/1691.

13. J. Tam, P. Tiruveedhula, and A. Roorda, "Characterization of single-file flow through human retinal parafoveal capillaries using an adaptive optics scanning laser ophthalmoscope," Biomed. Opt. Express **2**(4), 781–793 (2011), http://www.opticsinfobase.org/boe/abstract.cfm?URI=boe-2-4-781.

14. J. Tam and A. Roorda, "Speed quantification and tracking of moving objects in adaptive optics scanning laser ophthalmoscopy," J. Biomed. Opt. **16**(3), 036002 (2011), http://dx.doi.org/10.1117/1.3548880.

15. Z. Zhong, H. Song, T. Y. P. Chui, B. L. Petrig, L. Benno, and S. A. Burns, "Noninvasive measurements and analysis of blood velocity profiles in human retinal vessels," Invest. Ophthalmol. Vis. Sci. **52**(7), 4151–4157 (2011), http://www.iovs.org/content/52/7/4151.abstract.

16. M. J. Hogan, J. A. Alvarado, and J. E. Weddell, *Histology of the Human Eye* (W.B. Saunders Company, 1971).

17. Shinya Inoué, "Foundations of confocal scanned imaging in light microscopy," in *Handbook of Biological Confocal Microscopy*, J. B. Pawley, ed. (Springer, 1995), pp. 1–14.

18. D. Huang, E. A. Swanson, C. P. Lin, J. S. Schuman, W. G. Stinson, W. Chang, M. R. Hee, T. Flotte, K. Gregory, C. A. Puliafito, and J. G. Fujimoto, "Optical coherence tomography," Science **254**(5035), 1178–1181 (1991), http://www.sciencemag.org/cgi/content/abstract/254/5035/1178.

19. E. A. Swanson, D. Huang, M. R. Hee, J. G. Fujimoto, C. P. Lin, and C. A. Puliafito, "High-speed optical coherence domain reflectometry," Opt. Lett. **17**(2), 151–153 (1992), http://www.osa.org/abstract.cfm?URI=ol-17-2-151.

20. M. Wojtkowski, T. Bajraszewski, P. Targowski, and A. Kowalczyk, "Real-time in vivo imaging by high-speed spectral optical coherence tomography," Opt. Lett. **28**(19), 1745–1747 (2003), http://ol.osa.org/abstract.cfm?URI=ol-28-19-1745.

21. N. Nassif, B. Cense, B. H. Park, S. H. Yun, T. C. Chen, B. E. Bouma, G. J. Tearney, and J. F. de Boer, "In vivo human retinal imaging by ultrahigh-speed spectral domain optical coherence tomography," Opt. Lett. **29**(5), 480–482 (2004), http://ol.osa.org/abstract.cfm?URI=ol-29-5-480.

22. B. Cense, N. Nassif, T. Chen, M. Pierce, S. Yun, B. Park, B. Bouma, G. Tearney, and J. F. de Boer, "Ultrahigh-resolution high-speed retinal imaging using spectral-domain optical coherence tomography," Opt. Express **12**(11), 2435–2447 (2004).

23. W. Drexler and J. G. Fujimoto, "State-of-the-art retinal optical coherence tomography," Prog. Retin. Eye Res. **27**(1), 45–88 (2008). http://www.sciencedirect.com/science/article/pii/S1350946207000444.

24. B. Potsaid, B. Baumann, D. Huang, S. Barry, A. E. Cable, J. S. Schuman, J. S. Duker, and J. G. Fujimoto, "Ultrahigh speed 1050nm swept source / Fourier domain OCT retinal and anterior segment imaging at 100,000 to 400,000 axial scans per second," Opt. Express **18**(19), 20029–20048 (2010).

25. X. J. Wang, T. E. Milner, and J. S. Nelson. "Characterization of fluid flow velocity by optical Doppler tomography," Opt. Letters **20**(11), 1337–1339 (1995), http://ol.osa.org/abstract.cfm?URI=ol-20-11-1337.

26. S. Yazdanfar, A. M. Rollins, and J. A. Izatt, "Imaging and velocimetry of the human retinal circulation with color Doppler optical coherence tomography," Opt. Lett. **25**(19), 1448–1450 (2000), http://ol.osa.org/abstract.cfm?URI=ol-25-19-1448.

27. R. Leitgeb, L. Schmetterer, W. Drexler, A. Fercher, R. Zawadzki, and T. Bajraszewski, "Real-time assessment of retinal blood flow with ultrafast acquisition by color Doppler Fourier domain optical coherence tomography," Opt. Express **11**(23), 3116–3121 (2003).

28. B. White, M. Pierce, N. Nassif, B. Cense, B. Park, G. Tearney, B. Bouma, T. Chen, and J. F. de Boer, "In vivo dynamic human retinal blood flow imaging using ultra-high-speed spectral domain optical coherence tomography," Opt. Express **11**(25), 3490–3497 (2003).

29. Y. Zhao, Z. Chen, C. Saxer, S. Xiang, J. F. de Boer, and J. Stuart Nelson. "Phase-resolved optical coherence tomography and optical Doppler tomography for imaging blood flow in human skin with fast scanning speed and high velocity sensitivity," Opt. Lett. **25**(2), 114–116 (2000) http://ol.osa.org/abstract.cfm?URI=ol-25-2-114.

30. I. Grulkowski, I. Gorczynska, M. Szkulmowski, D. Szlag, A. Szkulmowska, R. A. Leitgeb, A. Kowalczyk, and M. Wojtkowski, "Scanning protocols dedicated to smart velocity ranging in spectral OCT," Opt. Express **17**(26), 23736–23754 (2009).

31. L. An, T. T. Shen, and R. K. Wang, "Using ultrahigh sensitive optical microangiography to achieve compre-

hensive depth resolved microvasculature mapping for human retina," J. Biomed. Opt. **16**(10), 106013–106013-9 (2011), http://link.aip.org/link/?JBO/16/106013/1.

32. Y. Hong, S. Makita, F. Jaillon, M. J. Ju, E. J. Min, B. H. Lee, M. Itoh, M. Miura, and Y. Yasuno. "High-penetration swept source Doppler optical coherence angiography by fully numerical phase stabilization," Opt. Express **20**(3), 2740–2760 (2012).

33. J. Barton and S. Stromski, "Flow measurement without phase information in optical coherence tomography images," Opt. Express **13**(14), 5234–5239 (2005).

34. A. Mariampillai, B. A. Standish, E. H. Moriyama, M. Khurana, N. R. Munce, M. K. K. Leung, J. Jiang, A. Cable, B. C. Wilson, I. A. Vitkin, and V. X. D. Yang, "Speckle variance detection of microvasculature using swept-source optical coherence tomography," Opt. Lett. **33**(13), 1530–1532 (2009), http://ol.osa.org/abstract.cfm?URI=ol-33-13-1530.

35. R. Motaghiannezam and S. Fraser, "Logarithmic intensity and speckle-based motion contrast methods for human retinal vasculature visualization using swept source optical coherence tomography," Biomed. Opt. Express **3**(3), 503–521 (2012), http://www.opticsinfobase.org/boe/abstract.cfm?URI=boe-3-3-503.

36. Y. Jia, O. Tan, J. Tokayer, B. Potsaid, Y. Wang, J. J. Liu, M. F. Kraus, H. Subhash, J. G. Fujimoto, J. Hornegger, and D. Huang, "Split-spectrum amplitude-decorrelation angiography with optical coherence tomography," Opt. Express **20**(4), 4710–4725 (2012).

37. J. Fingler, R. J. Zawadzki, J. S. Werner, D. Schwartz, and S. E. Fraser, "Volumetric microvascular imaging of human retina using optical coherence tomography with a novel motion contrast technique," Opt. Express **17**(24), 22190–22200 (2009).

38. L. Wang, Y. Wang, S. Guo, J. Zhang, M. Bachman, G. P. Li, and Z. Chen, "Frequency domain phase-resolved optical Doppler and Doppler variance tomography," Opt. Commun. **242**, 345–350 (2004). http://www.sciencedirect.com/science/article/B6TVF-4D8F6KC-1/2/248c1c0c32a9be950faa5260ae275c0e.

39. G. Liu, W. Qi, L. Yu, and Z. Chen, "Real-time bulk-motion-correction free Doppler variance optical coherence tomography for choroidal capillary vasculature imaging," Opt. Express **19**(4), 3657–3666 (2011).

40. S. Makita, F. Jaillon, M. Yamanari, M. Miura, and Y. Yasuno, "Comprehensive in vivo micro-vascular imaging of the human eye by dual-beam-scan Doppler optical coherence angiography," Opt. Express **19**(2), 1271–1283 (2011).

41. S. Zotter, M. Pircher, T. Torzicky, M. Bonesi, E. Götzinger, R. A. Leitgeb, and C. K. Hitzenberger, "Visualization of microvasculature by dual-beam phase-resolved Doppler optical coherence tomography," Opt. Express **19**(2), 1217–1227 (2011).

42. B. Hermann, E. J. Fernández, A. Unterhuder, A. F. Fercher, W. Drexler, P. M. Prieto, and P. Artal, "Adaptive-optics ultrahigh-resolution optical coherence tomography," Opt. Lett. **29**(18), 2142–2144 (2004), http://ol.osa.org/abstract.cfm?URI=ol-29-18-2142.

43. R. J. Zawadzki, S. S. Choi, S. M. Jones, S. S. Oliver, and J. S. Werner, "Adaptive optics-optical coherence tomography: optimizing visualization of microscopic retinal structures in three dimensions," J. Opt. Soc. Am. A **24**(5), 1373–1383 (2007), http://josaa.osa.org/abstract.cfm?URI=josaa-24-5-1373.

44. D. X. Hammer, N. V. Iftimia, R. D. Ferguson, C. E. Bigelow, T. E. Ustun, A. M. Barnaby, and A. B. Fulton, "Foveal fine structure in retinopathy of prematurity: an adaptive optics Fourier domain optical coherence tomography study," Invest. Ophthalmol. Vis. Sci. **49**(5), 2061–2070 (2008), http://dx.doi.org/10.1167/iovs.07-1228.

45. Q. Wang, O. P. Kocaoglu, B. Cense, J. Bruestle, R. S. Jonnal, W. Gao, and D. T. Miller, "Imaging retinal capillaries using ultrahigh-resolution optical coherence tomography and adaptive optics," Invest. Ophthalmol. Vis. Sci. **52**(9), 6292–6299 (2011), http://www.iovs.org/content/early/2011/01/17/iovs.10-6424.abstract.

46. R. J. Zawadzki, S. S. Choi, A. R. Fuller, J. W. Evans, B. Hamann, and J. S. Werner, "Cellular resolution volumetric in vivo retinal imaging with adaptive optics–optical coherence tomography," Opt. Express **17**(5), 4084–4094 (2009).

47. O. P. Kocaoglu, S. Lee, R. S. Jonnal, Q. Wang, A. E. Herde, J. C. Derby, W. Gao, and D. T. Miller, "Imaging cone photoreceptors in three dimensions and in time using ultrahigh resolution optical coherence tomography with adaptive optics," Biomed. Opt. Express **2**(4), 748–763 (2011), http://www.opticsinfobase.org/boe/abstract.cfm?URI=boe-2-4-748.

48. K. Kurokawa, K. Sasaki, S. Makita, M. Yamanari, B. Cense, and Y. Yasuno, "Simultaneous high-resolution retinal imaging and high-penetration choroidal imaging by one-micrometer adaptive optics optical coherence tomography," Opt. Express **18**(8), 8515–8527 (2010).

49. K. Sasaki, K. Kurokawa, S. Makita, and Y. Yasuno, "Extended depth of focus adaptive optics spectral domain optical coherence tomography," Biomed. Opt. Express **3**(10), 2353–2370 (2012).

50. E. J. Fernández, A. Unterhuber, B. Považay, B. Hermann, P. Artal, and W. Drexler, "Chromatic aberration correction of the human eye for retinal imaging in the near infrared," Opt. Express **14**(13) 6213–6225 (2006).

51. R. J. Zawadzki, B. Cense, Y. Zhang, S. S. Choi, D. T. Miller, and J. S. Werner, "Ultrahigh-resolution optical coherence tomography with monochromatic and chromatic aberration correction," Opt. Express **16**(11), 8126–8143 (2008).

52. R. J. Zawadzki, S. M. Jones, S. Pilli, S. Balderas-Mata, D. Y. Kim, S. S. Olivier, and J. S. Werner, "Integrated adaptive optics optical coherence tomography and adaptive optics scanning laser ophthalmoscope system

for simultaneous cellular resolution in vivo retinal imaging," Biomed. Opt. Express **2**(6), 1674–1686 (2011), http://www.opticsinfobase.org/boe/abstract.cfm?URI=boe-2-6-1674.

53. A. Unterhuber, B. Považay, B. Hermann, H. Sattmann, A. Chavez-Pirson, and W. Drexler, "In vivo retinal optical coherence tomography at 1040 nm - enhanced penetration into the choroid," Opt. Express **13**(9), 3252–3258 (2005).

54. L. Chen, "Control algorithms," in *Adaptive Optics for Vision Science: Principles, Practices, Design and Applications,* J. Porter, H. Queener, J. Lin, K. Thorn, and A. A. S. Awwal, eds. (Wiley-Interscience, 2006).

55. S. Makita, Y. Hong, M. Yamanari, T. Yatagai, and Y. Yasuno, "Optical coherence angiography," Opt. Express **14**(17), 7821–7840 (2006).

56. L. An and R. K. Wang, "In vivo volumetric imaging of vascular perfusion within human retina and choroids with optical micro-angiography," Opt. Express **16**(15) 11438–11452 (2008).

57. A. Szkulmowska, M. Szkulmowski, D. Szlag, A. Kowalczyk, and M. Wojtkowski, "Three-dimensional quantitative imaging of retinal and choroidal blood flow velocity using joint spectral and time domain optical coherence tomography," Opt. Express **17**(13), 10584–10598 (2009).

58. S. H. Yun, G. Tearney, J. F. de Boer, and B. Bouma, "Motion artifacts in optical coherence tomography with frequency-domain ranging," Opt. Express **12**(13), 2977–2998 (2004).

59. J. Walther, A, Krüger, M. Cuevas, and E. Koch, "Effects of axial, transverse, and oblique sample motion in FD OCT in systems with global or rolling shutter line detector," J. Opt. Soc. A. A **25**(11), 2791–2802 (2008), http://josaa.osa.org/abstract.cfm?URI=josaa-25-11-2791.

60. B. Park, M. C. Pierce, B. Cense, S. H. Yun, M. Mujat, G. Tearney, B. Bouma, and J. F. de Boer, "Real-time fiber-based multi-functional spectral-domain optical coherence tomography at 1.3 μm," Opt. Express **13**(11), 3931–3944 (2005).

61. P. Bedggood, M. Daaboul, R. Ashman, G. Smith, and A. Metha, "Characteristics of the human isoplanatic patch and implications for adaptive optics retinal imaging," J. Biomed. Opt. **13**(2), 024008–024008-7 (2008), http://link.aip.org/link/?JBO/13/024008/1.

62. D. M. Snodderly, R. S. Weinhaus, and J. C. Choi, "Neural-vascular relationships in central retina of macaque monkeys (Macaca fascicularis)," J. Neurosci. **12**(4), 1169–1193 (1992).

63. S. Yoneya and M. O. M Tso, "Angioarchitecture of the human choroid," Arch. Ophthalmol. **105**(5), 681–687 (1987), http://archopht.ama-assn.org/cgi/content/abstract/105/5/681.

64. H. Ishikawa, D. M. Stein, G. Wollstein, S. Beaton, J. G. Fujimoto, and J. S. Schuman, "Macular segmentation with optical coherence tomography," IOVS **46**(6), 2012–2017 (2005), http://dx.doi.org/10.1167/iovs.04-0335.

65. T. Fabritius, S. Makita, M. Miura, R. Myllylä, and Y. Yasuno, "Automated segmentation of the macula by optical coherence tomography," Opt. Express **17**(18), 15659–15669 (2009), http://www.opticsinfobase.org/oe/abstract.cfm?uri=oe-17-18-15659.

66. S. J. Chiu, C. A. Toth, C. Bowes Rickman, J. A. Izatt, and S. Farsiu, "Automatic segmentation of closed-contour features in ophthalmic images using graph theory and dynamic programming," Biomed. Opt. Express 3(5), 1127–1140 (2012), http://www.opticsinfobase.org/oe/abstract.cfm?URI=oe-18-18-19413.

67. V. Kajić, B. Považay, B. Hermann, B. Hofer, D. Marshall, P. L. Rosin, and W. Drexler, "Robust segmentation of intraretinal layers in the normal human fovea using a novel statistical model based on texture and shape analysis," Opt. Express **18**(14), 14730–14744 (2010).

68. Z136 Committee, *American National Standard for Safe Use of Lasers: ANSI Z136.1-2000* (Laser Institute of America, 2003).

69. T. Klein, W. Wieser, C. M. Eigenwillig, B. R. Biedermann, and R. Huber, "Megahertz OCT for ultrawide-field retinal imaging with a 1050nm fourier domain mode-locked laser," Opt. Express **19**(4), 3044–3062 (2011), http://www.opticsinfobase.org/oe/abstract.cfm?URI=oe-19-4-3044.

70. B. Potsaid, V. Jayaraman, J. G. Fujimoto, J. Jiang, P. J. S. Heim, and A. E. Cable, "MEMS tunable VCSEL light source for ultrahigh speed 60kHz - 1MHz axial scan rate and long range centimeter class OCT imaging," Proc. SPIE **8213**, 82130M–82130M-8 (2012).

71. S. S. Hayreh, "The choriocapillaris," Graefe's Archive for Clinical and Experimental Ophthalmology **192**(3), 165–179 (1974), http://dx.doi.org/10.1007/BF00416864.

72. R. W. Flower, A. W. Fryczkowski, and D. S. McLeod, "Variability in choriocapillaris blood flow distribution," Invest. Ophthalmol. Vis. Sci. **36**(7), 1247–1258 (1995), http://www.ncbi.nlm.nih.gov/pubmed/7775102.

73. R. W. Flower, E. Peiretti, M. Magnani, L. Rossi, S. Serafini, Z. Gryczynski, and I. Gryczynski, "Observation of erythrocyte dynamics in the retinal capillaries and choriocapillaris using ICG-loaded erythrocyte ghost cells," Invest. Ophthalmol. Vis. Sci. **49**(12), 5510–5516 (2008), http://www.iovs.org/content/49/12/5510.long.

74. C. Torti, B. Považay, B. Hofer, A. Unterhuber, J. Carroll, P. Kurt Ahnelt, and W. Drexler, "Adaptive optics optical coherence tomography at 120,000 depth scans/s for non-invasive cellular phenotyping of the living human retina," Opt. Express **17**(22), 19382–19400 (2009).

1. Introduction

The retinal and choroidal vasculature play significant roles in maintaining visual function. Specifically, arteries transport oxygen and nutrients, and veins return carbon dioxide and cellular waste products. Hence, the malfunction and malformation of the vasculature results in significant visual impairment [1]. For instance, retinal layers are damaged by vessel occlusion, and they never regenerate. Furthermore, it is known that several severe eye diseases, such as glaucoma, age-related macular degeneration, and diabetic retinopathy, are associated with physiological and structural vascular changes [1–4]. Especially in age-related macular degeneration and diabetic retinopathy, angiogenesis is found at the capillary level [3,5]. Early detection and better diagnosis are the key to preventing such significant visual impairment.

Vascular imaging techniques have been developed to detect both physiological and structural changes. For instance, fluorescein angiography (FA) and indocyanine angiography (ICGA) have been widely used in retinal and choroidal vascular imaging as a part of clinical routines. These angiograms detect not only structural changes but also physiological changes. However, the FA and ICGA have risks of adverse reactions to the dye injection [6,7]. As a non-invasive method, retinal functional imager (RFI, Optical Imaging Ltd., Israel) is known to image structural vascular changes with the help of motion contrast and a selective illumination wavelength [8], which allows quantitative transversal blood velocity assessment and qualitative oximetric imaging at the capillary level.

Although, as exemplified by the above-mentioned modalities, the physiological and structural vascular changes have been investigated in details, the lateral resolution is limited by ocular monochromatic aberrations. This limitation has been overcome by adaptive optics scanning laser ophthalmoscopy (AO-SLO) [9], which is a non-invasive and high-resolution imaging technique. AO-SLO has been used for vascular imaging at the cellular level by dynamically correcting ocular monochromatic aberrations [10–15], which has enabled individual cell tracking including that of leukocytes and erythrocytes [10, 11, 13–15], and has enabled motion contrast to enhance the visibility of small retinal capillaries [12–14]. The lateral resolution of AO-SLO is high enough to image all retinal capillaries, which are typically around 5 μm in diameter [1].

However, the human retinal and choroidal vasculature is known to have a dense and complex three-dimensional (3-D) structure [1, 16]. And hence the application of optical coherence tomography (OCT), which possesses higher depth resolution than AO-SLO [17–19], would provide further detailed vascular structure. In addition, OCT has higher sensitivity, typically better than 90 dB. OCT has been shown to have powerful utility in ophthalmology owing to its high speed, high sensitivity, and high resolution [20–24].

Since the development of Doppler OCT [25–28], also known as optical Doppler tomography, several OCT-based methods have been used for 3-D non-invasive vasculature mapping at the capillary level. These methods include those based on the phase-difference between B-scans [29–32], speckle variance [33–35], amplitude decorrelation [36], phase variance [37], Doppler variance [38,39], and a dual-beam-scan technique [40,41]. Although these OCT-based methods reveal the three-dimensional micro-vasculature, the lateral resolution is again limited by ocular monochromatic aberrations, as in the case of the non-AO ophthalmoscope, and ocular chromatic aberrations.

AO-OCT is a state-of-the-art technology that allows microscopic investigation of the retinal and choroidal vasculature with extremely high lateral and axial resolution [42–48]. AO-OCT has been used in the structural investigation of three-dimensional micro-vasculature [43–45].

In this paper, to further improve micro-vascular imaging in the retina and choroid, we demonstrate Doppler OCT with AO, so called adaptive-optics optical coherence angiography (AO-OCA). In the method, we used several techniques, such as a moderate extension of depth of focus by a spherical aberration [49], a high-sensitive Doppler measurement by calculating the

phase difference between B-scans, a modified bulk motion correction method, and some image post-processing. The performance of several bulk motion correction methods are quantitatively compared. Microscopic and macroscopic retinal and choroidal vascular imaging is presented. In addition, *in vivo* choriocapillaris and choroidal capillary imaging is demonstrated.

2. Method

2.1. System

A custom-made system was used in this study for adaptive-optics spectral-domain OCT (AO-SDOCT). This AO-SDOCT is nearly identical to our previous system, but has higher resolution and speed owing to an achromatizer and a new line sensor. Since the details of the previous system is described elsewhere [48, 49], here we give a brief summary of the system.

Our adaptive-optics retinal scanner is a reflection type with a single deformable mirror. A custom-designed broadband achromatizer is used. The general concept of an achromatizer was described by Fernández *et al.* [50]. We designed the achromatizer to cancel not only for the longitudinal chromatic aberration (LCA) of the eye but also for the LCA of the system. The optical design of the achromatizer is shown in Fig. 1(a). The numerical simulation showed the axial chromatic focal shift was corrected less than 3 μm at the wavelength bands of 970 nm and 1070 nm as shown in Fig. 1(b).

The achromatizer is located between the input collimator and a dichroic mirror as proposed by Zawadzki *et al.* [51]. This configuration is utilized to prevent surface reflection from the achromatizer to the SHWS. In addition, the dichroic mirror splits a back-scattered sample beam to the fiber tip and to a Shack-Hartmann wavefront sensor (SHWS, HASO32, Imagine Eyes, Orsay, France). As demonstrated by Zawadzki et al. [52], this configuration allows the usage of two difference wavelengths for probe and beacon beams.

The SD-OCT sub-system consists of a spectrometer with an InGaAs line sensor driven at a line-rate of 91,911 lines/s (SUI1024LDH2, Sensors Unlimited, Inc., Goodrich, NC). The OCT interferometer is a fiber based Michelson interferometer with a 50:50 fiber coupler. The light source is an superluminescent diode (SLD, Superlum Ltd., Ireland) with a center wavelength of 1020 nm, which has deeper penetration than a center wavelength of 840 nm [53]. The bandwidth of the SLD is 106 nm and the axial resolution was measured to be 4.8 μm (in tissue), while the pixel separation was 2.5 μm (in tissue). The system sensitivity was measured to be 81.5 dB without correction of system aberration. After measuring the sensitivity, the root-mean-square (RMS) wavefront error was measured by using a model eye with a paper target, and was 0.54 μm. Note that, because of the large beam diameter (7.4 mm), system aberration deteriorated this measured system sensitivity [48]. The true sensitivity under closed-loop adaptive-optics operation is expected to be higher than this measured value, although it cannot be experimentally defined.

The post-processing was carried out by a PC with a CPU (Intel(R) Core(TM) 2 Duo Processor T9550 with 6MB L2 Cache, and 2.66 GHz clock speed) and 8 GB memory (DDR3-SDRAM 2GB × 4). All of post-processing was implemented by LabVIEW 2011 on 64-bit Windows 7 operating system.

2.2. Adaptive-optics controller

The aberrations were measured by the SHWS and corrected by a deformable mirror (DM) with 52 megnetomotive actuators (Mirao52e, Imagine Eyes). A laser diode with wavelength of 700 nm (HL7001MG, Thorlabs Inc., NJ) was used as an adaptive-optics beacon. The adaptive-optics control software was written in LabVIEW using adaptive-optics control SDK (Imagine Eyes).
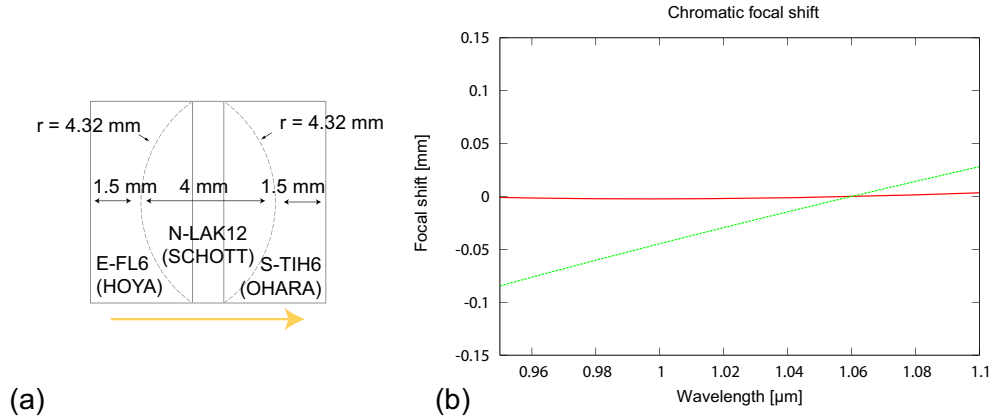
Fig. 1. (a) Optical design of achromatizer. An yellow arrow indicates the beam direction from the fiber tip to the retina. (b) The chromatic focal shift with the achromatizer (red solid line) and without the achromatizer (green dashed line).

An integral controller with target slopes described as follows is used for the closed-loop control. Here a vector of command voltages (command vector) of the DM, $\mathbf{v}_{t+T}$, at time $t+T$ is defined as [54]

$$\mathbf{v}_{t+T} = \mathbf{v}_t - \alpha \mathbf{A}^+ \left(\mathbf{s}_T - \mathbf{s}_{target} \right), \tag{1}$$

where $\mathbf{v}_t$ is the command vector at time t, and $\mathbf{s}_T$ is the measured slope vector with the exposure time of T, whose dimension is equal to the number of subapertures within a pupil measured by the SHWS. $\mathbf{s}_{target}$ is a target slope vector. The pseudo inverse matrix of an influence matrix $\mathbf{A}^+$ was obtained by singular value decomposition. Using this controller, an arbitrary wavefront can be set as a target wavefront and reconstructed by the adaptive-optics.

In this study, we used the large beam diameter, and hence, the depth of focus becomes significantly smaller than the total thickness of the retina and choroid, which is around 0.6 mm. The expected depth of focus derived by a numerical simulation, which was defined by the FWHM in depth, was 52.7 μm. In order to extend the depth of focus, we introduced a spherical aberration (SA) by modulating the phase distribution of the pupil [49]. Specifically, the SA was 0.89 μm in peak-valley (PV). This value was selected to have 3-times longer focal range (156 μm) in theory and it provided a stable measurement condition. The defocus was adjusted to focus on the photoreceptors.

2.3. Doppler optical coherence angiography

2.3.1. Doppler shift calculation

Doppler OCT provides motion-specific contrast by detecting Doppler frequency shifts occurred by moving particles. In our methods, Doppler OCT technology is employed for the selective contrast of micro-vasculatures. In conventional phase sensitive Doppler OCT, the phase differences between adjacent A-lines are calculated. For ocular vasculature imaging, bulk motion correction is commonly performed to obtain bidirectional Doppler shifts of moving scatterers $\Delta\phi_i(z)$. Then, Doppler power imaging, in which the image pixel value is determined by the squared power of the Doppler shift $\Delta\phi_i^2(z)$, has enabled high-contrast vascular imaging.

Although large vascular networks are imaged by conventional Doppler OCT, it is still difficult to image small capillaries because the capillaries have low flow velocity, lay nearly perpendicular to the probe beam, and have small diameters [1, 2]. To obtain higher sensitivity to the

capillary flow, a long time separation and high-resolution imaging are required. For the long time separation, we calculated phase differences between two adjacent B-scans [29, 31, 32] and the time separation of 1.4 ms was achieved. To improve the lateral resolution, the ocular monochromatic aberrations were corrected by adaptive-optics.

2.3.2. Bulk motion correction

A constant phase offset, ϕ_B, owing to sample bulk motion and unstable scanning, disturbs the Doppler measurement. Methods that use the mode or mean of the Doppler shift to detect and cancel the bulk motion have been demonstrated [28, 55–57].

However, with the long time separation such as that in our protocol, many small capillaries can be detected, and hence the static regions become small. This disturbs the above-mentioned standard methods for bulk motion correction. This is because the detection accuracy of the constant phase offset relies on the selection of the static tissues. In other words, by selecting the static regions effectively, we can improve the estimation accuracy. In this paper, we used the OCT signal intensity as a weight function to effectively select the static tissue [28]. In addition, this estimator was extended into a complex form to have higher robustness. The weight function provides an appropriate selection of the static tissues of the eye for the following reasons. First, the OCT signal is, in SD-OCT, weaker in a dynamic region with stronger motion, such as in blood vessels [58, 59]. Second, the static retinal structures including photoreceptors, the retinal pigment epithelium (RPE), and nerve fiber layers are strong scatterers and hence have high OCT signal intensity. For instance, the photoreceptors and RPE typically have a mean signal-to-noise ratio (SNR) larger than 20 dB, while the choroid and retinal capillaries has an SNR of around 15 dB or less. Third, because the random phase noise depends on the SNR [60], the phase value is more reliable with the higher SNR. Under the above circumstances, the intensity-weighted mean estimator is a good candidate for the bulk motion correction.

Another problem associated with the Doppler measurement protocol using a long time separation is frequent phase wrapping. This is because the measurable maximum Doppler velocity is small. Although this is not problematic in the case of the mode estimator [55], the phase wrapping disturbs the mean estimation [28, 56] and it should be corrected by some means. And hence, in this paper, we calculated the mean value in complex form, because this complex mean is robust for the phase wrapping.

Our mean estimator is described as

$$\phi_B \equiv \mathrm{Arg}\left[\sum_j S_i(j) S_{i+1}^*(j)\right], \tag{2}$$

where ϕ_B is the estimated sample bulk motion, $S_i(j)$ is the complex OCT signal at the j-th depth pixel in the i-th A-line and the superscript $*$ denotes the complex conjugate. It is noteworthy that the amplitude of $S_i(j) S_{i+1}^*(j)$ is used as a weight of this mean calculation. This weight takes a larger value for a stronger OCT signal.

This proposed method has additional advantages other than the robustness to the phase wrapping occurred by a large bulk motion. First, the estimation is robust even in the case with large blood vessels, in which the blood flow velocity far exceeds the maximum velocity range. Since, in such large blood vessels, the phase values appear as random values with a zero-mean, the complex mean estimator is less sensitive to the blood flow but selectively sensitive to the bulk motion of the eye. Second, it is significantly faster in computation than the mode estimator and the other recently proposed iterative methods [31, 32, 55]. Third, it does not need to apply intensity threshold, and hence is a totally linear operation [57].

In order to evaluate the proposed mean estimator, the performances of the mean and mode bulk-motion estimators are quantitatively compared in Section 3.1.

2.4. Image post-processing

2.4.1. Volume registration

Multiple volumes taken at a single retinal location are registered to each other semi-automatically. Since a similar method was demonstrated by Kocaoglu *et al.*. [47], we only briefly summarize the method.

First each volume is flattened to the inner/outer segment junction (IS/OS) by detecting the IS/OS employing customized edge detection and an iterative smoothing algorithm [55]. Second, the transversal shifts among volumes are detected and corrected using a phase-correlation based-registration algorithm. In detail, the *en face* slices of photoreceptors are extracted from each volume. These *en face* images are segmented into several strips along the fast-scan axis. The transversal motion of the strips relative to a proper reference image is detected by the phase-correlation based registration algorithm. Some segmented strips with small correlation coefficients are rejected. Finally, a set of motion-corrected volumes is obtained.

2.4.2. Volume averaging

In some of the measurement protocols used in this study, the OCT intensity and Doppler power volumes at a single retinal location are averaged to enhance the contrast after being co-registered. Note that the Doppler power volumes are averaged after applying a mask that replaces the phase value with the value zero if the SNR of the corresponding OCT intensity is less than 10 dB.

2.4.3. Volume stitching

A wider field of view (FOV) volume is obtained by stitching multiple volumes at several retinal positions, similar to the method presented by Zawadzki *et al.* [46]. Since each volume had been flattened to the IS/OS, only the transversal shifts are manually determined. To avoid blurring, the volumes are not further averaged in the overlapped regions. In Sections 3.2 and 3.3, the volume with the highest average intensity was displayed at each location, while in Section 3.4, the volume with the best subjective image quality was displayed.

The SNR varies among the measurement data sets. To reduce the variability of the contrast among the intensity volumes, the range of pixel brightness of each volume is normalized to have the same maximum brightness value.

In general, the FOV of a single patch is limited by field aberrations originating from the limited size of the isoplanatic patch of ocular optics [61]. This small patch size sometimes results in the absence of or only a very small overlapped region among neighboring volumes. It finally results in failure of the volume stitching.

In some protocols, to avoid this failure, a set of volumes that have a relatively wide FOV but low resolution are obtained before acquiring the high-resolution but small FOV volumes. A mosaic of the wide FOV patches is first created, and the small FOV volumes are then co-registered to this mosaic. This multi-scale protocol enables more accurate volume registration.

2.4.4. Retinal layer segmentation

In the region close to the fovea, the retinal capillaries are known to have laminar distributions [1, 16, 62] except within the nerve fiber layer (NFL) and ganglion cell layer (GCL), in which capillaries have relatively complex three-dimensional capillary plexus [62]. Beneath the RPE, the choriocapillaris is connected to the pre-capillary arterioles and post-capillary venules in the Sattler layer [63]. Hence, the depth-resolved *en face* projection would provide intuitive understanding of the three-dimensional vascular structures.

To generate *en face* projections, we first segmented the retina and choroid into several layers by employing a customized algorithm for edge detection and smoothing.

In detail, we first average several neighboring B-scans in an OCT volume to reduce speckles. Specifically, in Sections 3.2 and 3.4, we average 17 B-scans in an averaged OCT volume. On the other hand, in Section 3.3, we average 60 B-scans in a non-averaged wide-field OCT volume that is generated after volume stitching. Here the 60 B-scans cover a 0.3-degree FOV, and we assume the laminar structure does not significantly vary within this 0.3-degree FOV. Then, using the sets of averaged B-scans, the following layer interfaces are automatically segmented by detecting the minimum or maximum of local gradients of the OCT intensity; i.e., the interface between the inner limiting membrane and NFL (ILM/NFL), the interface between the NFL and GCL (NFL/GCL), the interface between the inner nuclear layer and the outer plexiform layer (INL/OPL) and the interface between the RPE and choroid (RPE/choroid). In addition, the interface between the inner plexiform layer and INL (IPL/INL) is manually segmented.

Although the simple segmentation algorithm presented above would not be applicable to some clinical cases, several established alternative also can be used for the same purpose [64–67].

2.4.5. *En face* projections

In the retina, on the basis of the segmentation described in Section 2.4.4, we generate *en face* projections of four independent retinal layers, which are denoted as an NFL projection, GCL+IPL projection, IPL/INL projection, and INL/OPL projection.

The NFL projection is generated by averaging a retinal section between the ILM/NFL and NFL/GCL interfaces, and hence this projection contains the NFL. The GCL+IPL projection is generated by averaging a retinal section between the NFL/GCL and IPL/INL interfaces, and hence, it contains the GCL and IPL. The IPL/INL projection is generated by averaging several depth pixels centered on the IPL/INL interface. The INL/OPL projection is generated by averaging several depth pixels centered on the INL/OPL interface.

For the IPL/INL and INL/OPL projections, we manually set the number of depth pixels, which are used for averaging. Specifically, in Section 3.2, we average seven and ten depth pixels (17.2 and 24.6 μm in tissue) for the IPL/INL and INL/OPL projections, respectively. On the other hand, in Section 3.3, we average eight and nine depth pixels (19.7 and 22.2 μm in tissue) for the IPL/INL and INL/OPL projections, respectively. Because the number of depth pixels are reduced in the region close to the fovea because of the thinner retinal layer, the number is set to be reduced if the depth position of the upper boundary exceeds the NFL/GCL interface.

In the choroid, we generate *en face* projections of four independent choroidal layers, which are denoted as projections CC1 to CC4. These projections are segmented and numbered from the RPE/choroid interface, and they have thickness of a few micrometers. Specifically, in Section 3.2 and 3.4, the thickness of each projection is three pixels (7.4 μm in tissue). In Section 3.3, the thickness is two pixels (4.9 μm in tissue).

The *en face* projections are generated for the OCT intensity and Doppler power respectively. The *en face* projections of Doppler power images are further denoised by a transversal moving average filter with kernel size of 3 pix (fast) $\times$ 3 pix (slow) in Section 3.2, 2 pix (fast) $\times$ 2 pix (slow) in Section 3.3 and 3 pix (fast) $\times$ 5 pix (slow) in Section 3.4.

2.5. *Measurement protocol*

Three eyes of three healthy subjects are involved in this study. All eyes are myopic. The participants' characteristics are summarized in Table 2.5.

Informed consent was obtained from all subjects. The protocol conformed to the Declaration of Helsinki, and it was approved by the Institutional Review Board of the University of Tsukuba. Prior to measurement sessions, two drops of 0.5% tropicamide and 0.5% phenylephrine were applied for pupil dilation and cycloplegia.

The optical powers were 1.3 mW for the probing beam and 90 μW for the beacon beam. According to the safety limits defined by the American National Standard Institute [68], the maximum permissible radiant powers are 1.7 mW for the probing beam and 399 μW for the beacon beam with an exposure time of 10 seconds, assuming the eye was illuminated by only one of the two beams. In order to account for the simultaneous multiple beam exposure, the total fractional powers respect to the maximum permissible radiant power should be less than 1.0. In our case, it was 1.3 mW / 1.7 mW + 90 μW/ 399 μW = 0.99. And hence our measurement configuration satisfies the safety standard.

Table 1. Participants' characteristics. ID is the subject ID, Sph and Cyl are spherical and cylindrical refractive errors in diopters and L/R indicates the left (L)/right (R) eye.

ID	Sph	Cyl	L/R	Age	Axial eye length
A	-7.3 D	-0.3 D	R	25	26.24 mm
B	-6.6 D	-0.4 D	R	23	27.52 mm
C	-4.0 D	-0.3 D	R	26	25.73 mm

Three scanning protocols summarized in Table 2.5 were used. In protocol A, two sequential volumes were acquired at a speed of 2.8 volumes/s in a single measurement data set. In protocols B and C, nine sequential volumes were acquired at a speed of 5.6 volumes/s in a single measurement data set. Multi-scale measurement described in Section 2.4.3 was performed with protocols A and B. Highly sensitive measurement to be described in Section 3.4 was performed with protocol C.

The fixation target, which was a grid pattern on a piece of paper, was used to lead the subject to given eccentricities. In the measurement, the eccentricity was set at 3 degrees inferior and 1.5 degrees nasal in Sections 3.2 and 3.4. For the wide FOV imaging described in Section 3.3, the eccentricity was changed in 0.5-degree steps within a 5-degree-wide field.

The measurement was performed in less than 2.5 hours per day, and there were typically 60 data sets in a day.

Table 2. Summary of scanning protocols. The fractional displacement is the separation between adjacent B-scans with respect to the $1/e^2$ beam diameter of the probe. The minimum velocity is estimated for an SNR of 20 dB.

Protocol ID	Image size [pix] (fast × slow)	FOV [degree] (fast × slow)	Speed [vol/s]	Fractional displacement	Min. velocity [mm/s]
Protocol A	256 × 256	1.3 × 1.3	2.8	0.43	0.024
Protocol B	128 × 128	0.65 × 0.65	5.6	0.43	0.033
Protocol C	128 × 128	0.65 × 0.33	5.6	0.22	0.033

3. Result

3.1. Bulk motion correction

To quantitatively compare the performances of the mean and mode bulk motion estimators, we scanned an eye of subject A with scanning protocol B. The bulk motion was estimated using the mean and mode estimators, and to cancel the bulk phase occurred by the motion, the estimated
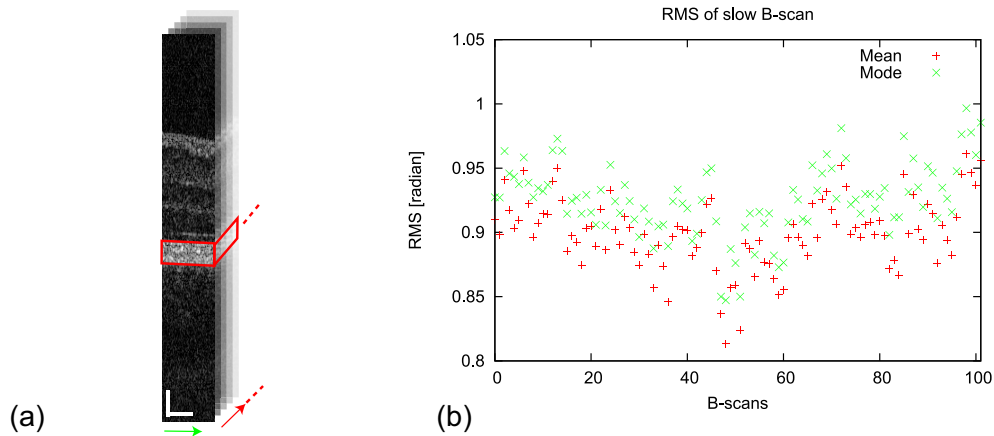
Fig. 2. (a) An example of the OCT volume used to evaluate the performance of bulk motion correction. The red box represents the region of interest. The red arrow indicates the slow-scan direction, and the blue arrow indicates the fast-scan direction. (b) The RMS of phase differences for each B-scan. '+' and '×' respectively indicate the RMS obtained with mean and mode motion estimators.

bulk motion phase was subtracted from the original Doppler phase shift. Since the Doppler shift is bidirectional, the RMS of the Doppler shifts was used as a measure of the performance of the motion correction. To obtain the statistics, a static region with strong scattering from the IS/OS to RPE/choroid interface was used as a region of interest as shown in Fig. 2(a).

Figure 2(b) shows the distribution of the RMS of the Doppler shift for each B-scan. In all B-scans, the RMS obtained by the mean estimator was smaller than that obtained by the mode estimator. The RMS of the Doppler shift of the whole region of interest was 0.90 rad for the mean estimator and 0.93 rad for the mode estimator. These results indicate that the mean estimator provides better bulk motion correction than the mode estimator.

3.2. Microscopic structures in the retina and choroid

We scanned subject A with scanning protocol B. The mean of the residual RMS wavefront error was 0.14 μm.

In the image post-processing, the volume registration and averaging were performed as described in Sections 2.4.1 and 2.4.2. An example of the high-contrast projection at the photoreceptor layer obtained in this process is shown in Fig. 3(a). The layer segmentation as described in Section 2.4.4 was then performed. The corresponding layers are indicated in Fig. 3(b). Finally, two volumes were stitched, and the *en face* projections were generated as described in Sections 2.4.3 and 2.4.5. The post-processing computation took around 10 minute and was followed by manual volume alignment process taking around an hour.

The depth-resolved retinal capillaries were observed in the intensity and Doppler power images as shown in Fig. 4(a). In the GCL and IPL projection, a relatively large blood vessel was imaged. No corresponding structure was observed at deeper projections. At the IPL/INL boundary, the retinal capillary bed was observed in the Doppler power image, which provided higher specificity of the capillaries than the corresponding intensity image. At the INL/OPL boundary, the high contrast retinal capillary bed was observed in both the intensity and Doppler power images. Here the hyper scatterers, which would mainly be red blood cells, had sufficient contrast to discriminate the capillaries from the static tissue.

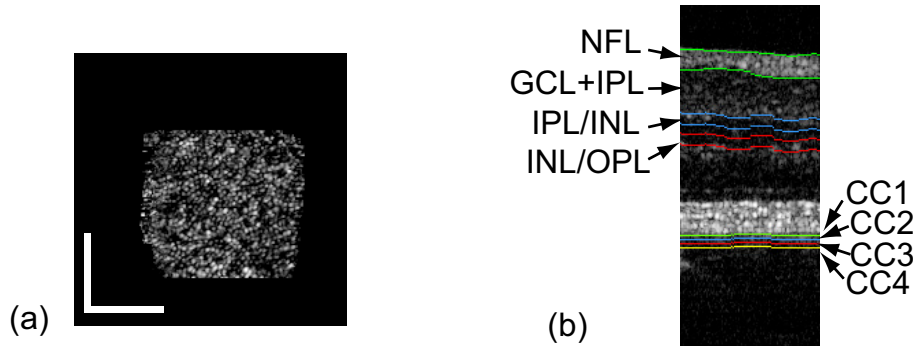On the other hand, in the choroid, the intensity and Doppler power images had different

Fig. 3. (a) *Enface* projection of photoreceptors. (b) Representative B-scan image with segmentation results. The corresponding depths are indicated by black arrows. A white bar indicate 100 μm.
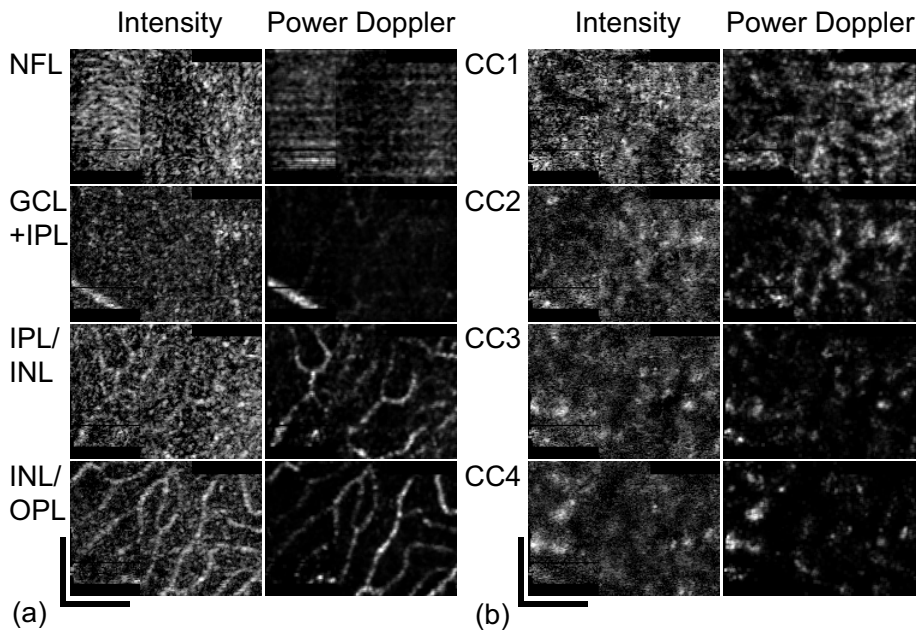

Fig. 4. (a) *Enface* projections of retinal capillaries. (b) *Enface* projections of the chori-ocapillaries layer and choroidal capillary in the Sattler layer. A black bar indicates 100 μm.

contrasts as shown in Fig. 4(b). Although Doppler power images showed the capillary patterns in projections CC1 and CC2, the corresponding patterns were hardly observed in the intensity images.

3.3. Macroscopic retina and choroid

Wide-FOV imaging was performed for the investigation of macroscopic retinal and choroidal structures with high resolution. Subject A was scanned with scanning protocols A and B. We performed 237 data sets in total over 4 days. In order to generate a wide field mosaic, we manually selected 149 data sets, which were not suffered by significant involuntary eye motion.
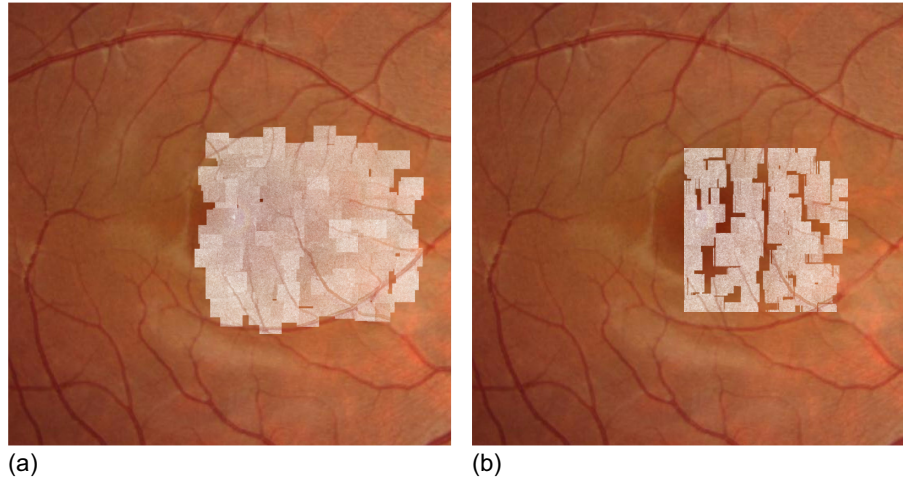
Fig. 5. (a) Measured area in the fundus image (5 mm × 5 mm). (b) Measured area after averaging and cropping

Twenty data sets were obtained with protocol-A, and the other 129 data sets were obtained with protocol B. The mean of residual RMS wavefront error was 0.145 μm.

In the image post-processing, the volume stitching described in Section 2.4.3 was first performed. The layer segmentation described in Section 2.4.4 was then performed. The volume registration and averaging was performed as described in Sections 2.4.1 and 2.4.2. Finally, a region of 1.5 mm × 1.5 mm was cropped for display. The measured area and cropped area are shown in Fig. 5. The post-processing computation took around 11 hours and was followed by manual volume alignment process taking around 18 hours.

Figures 6(a)-6(f) show the wide field and high resolution retinal capillaries. Laminar capillary beds at the shallow and deep boundaries of the INL are clearly visualized in Figs. 6(c)-6(f). The thicker capillary networks were found at the deep boundary of the INL. In addition, the retinal capillaries in the GCL and IPL had a non-laminar formation as shown in Media 1 and Media 2, which are fly-through movies of retinal capillary networks in the intensity and Doppler power images, respectively. The observations agree with the anatomical and histological findings [1, 62].

In the choroid, the *en face* projections of the choriocapillaris were generated from the RPE/choroid interface to a deeper layer with 5- μm (2-pixel) thickness as shown in Figs. 6(g) and 6(h). The smaller, complex, and dense capillary patterns were observed in the Doppler power image. However, only a cloudy pattern was observed in the intensity image similar to the microscopic observation. A three-dimensional structure can be viewed in the fly-through movies of intensity (Media 3) and Doppler power (Media 4), which are from the RPE/choroid interface to 100-μm (30-pixel) below the interface.

3.4. Choriocapillaris imaging

To demonstrate choriocapillaris imaging, three eyes of three subjects (subjects A, B and C) were scanned with protocol C, which has higher Doppler sensitivity than the other protocols. The mean of residual RMS wavefront errors was 0.09 μm, 0.09 μm, and 0.13 μm for subjects A, B, and C respectively.

In the image processing, the volume registration, averaging and layer segmentation were performed as described in Sections 2.4.1, 2.4.2, and 2.4.4. Finally, two or three volumes were
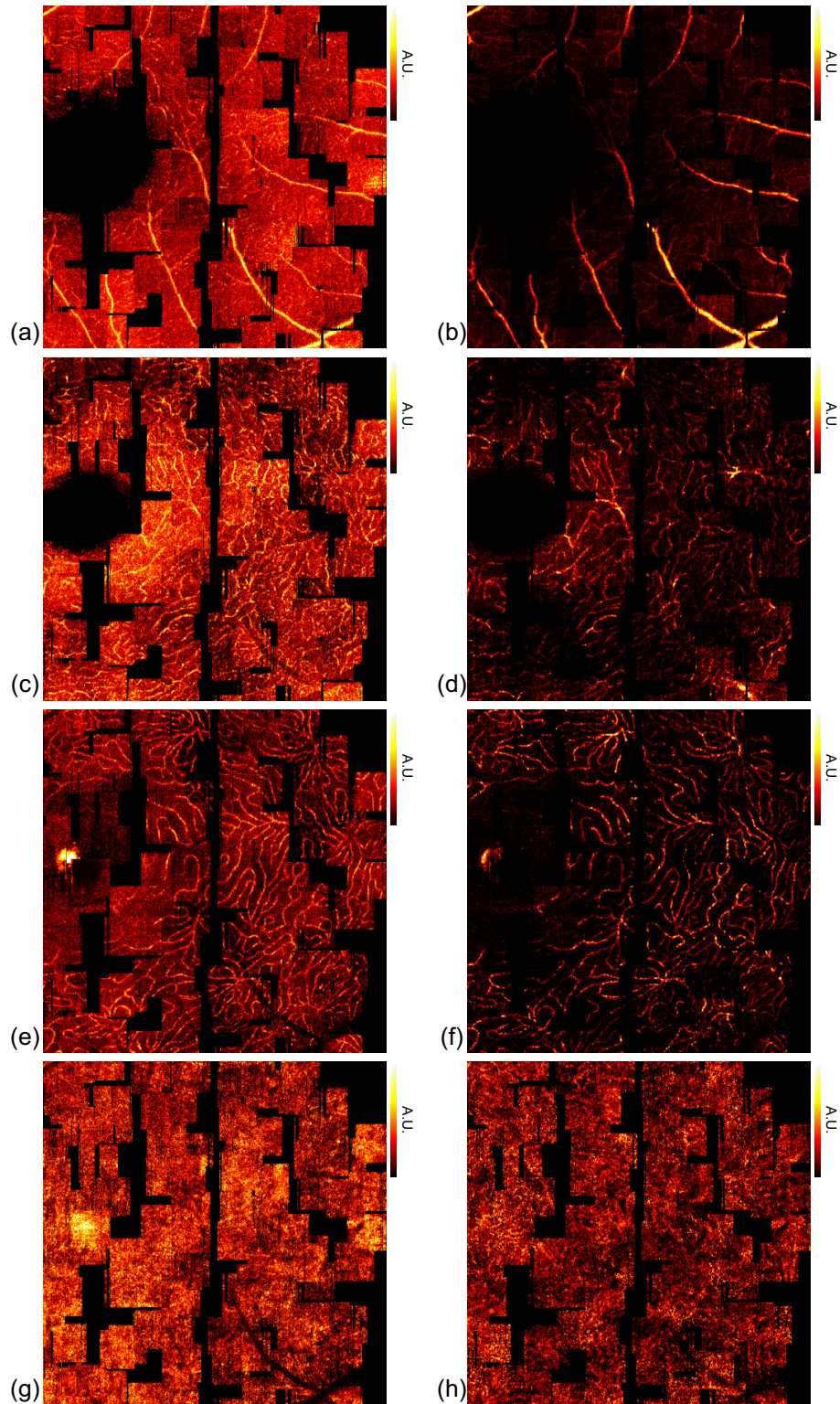
Fig. 6. Wide-field *en face* projections of intensity (left column) and Doppler power (right column) images at different depths of the GCL and IPL ((a) and (b)), IPL/INL boundary ((c) and (d)), INL/OPL boundary ((e) and (f)) and choriocapillaris ((g) and (h)).
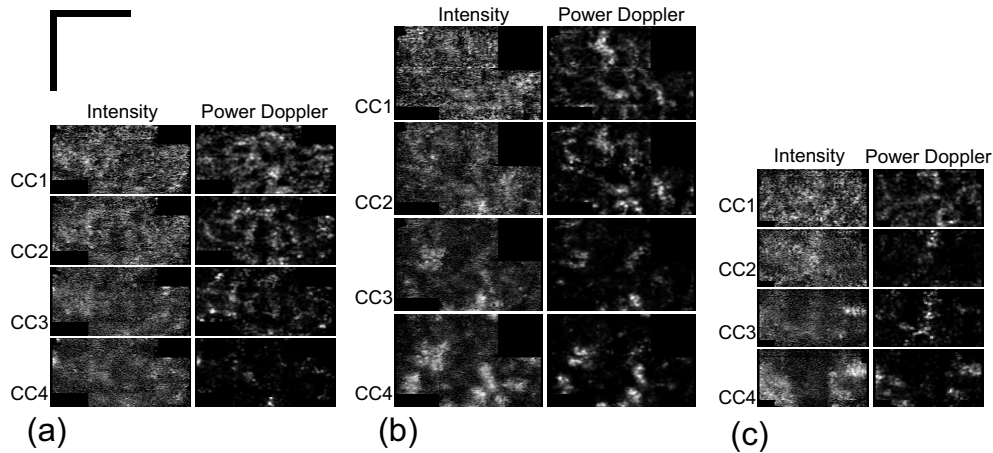
Fig. 7. (a)-(c) *Enface* projections of the choriocapillaris and Sattler layers at different depths for Subjects-A, B and C. A black bar indicates 100 μm.

stitched and the *en face* projections of the choroid were generated. The post-processing computation took around 10 minute and was followed by manual volume alignment process taking around an hour.

The same tendency was confirmed for all three eyes; the capillary patterns were successfully observed in the Doppler power images as shown in Fig. 7, while the corresponding patterns were not clearly observed in the intensity images.

4. Discussion

4.1. Involuntary eye motion

The current study has several limitations. The most severe limitation is that of involuntary eye motion. For high-sensitivity Doppler imaging, a highly dense scanning protocol (i.e., a protocol with a smaller fractional displacement) is required. Since the higher density of scanning requires a longer measurement time, the imaging is more easily disturbed by involuntary eye motion. For instance, the success rate of high-density scanning (protocol C) in our study was 27%, while the rates for protocols A and B were 95% and 72% respectively. Unfortunately, the current success rate of high-density scanning is low. However, this problem will be easily overcome by high-speed OCT imaging technology [69, 70].

4.2. Capillary imaging

4.2.1. Retinal capillary imaging

Although the incident beam was focused on the photoreceptors in our study, three-dimensional comprehensive capillary imaging through the whole depth of the retina was demonstrated. This can be accounted for by the extended depth of focus due to introducing SA to the target wavefront of the adaptive-optics closed loop [49].

In the case of the retina, the intensity and Doppler power images showed similar contrasts for the retinal capillaries as shown in Figs. 4 and 6. However, the structures visible in the two modalities are not always the same because of the difference in the contrast mechanisms of the modalities. For instance, the contrast of an intensity image depends on the scattering properties of tissues and blood cells. On the other hand, the contrast of a Doppler power image depends on the capillary blood flow velocity and its angle in addition to the phase noise. Hence, the

intensity and Doppler power images complement each other in clarifying the structural and physiological properties of the vasculature.

4.2.2. Choriocapillaris

Although choriocapillaris imaging has been reported using FA [71] and ICGA [72], neither of the methods provide the microscopic structure of the choriocapillaris. ICG was also used to investigate the vascular dynamics of the choriocapillaris [73]. The investigation requires artificial cells containing ICG and is thus an elaborate procedure, and is not approved for human investigation. In addition, the limited depth resolution of FA and ICGA prohibits the three-dimensional investigation of the choriocapillaris. Furthermore FA and ICGA are not noninvasive methods and induce some adverse reactions.

The issues of the limited transversal and depth resolutions can be overcome by AO-OCT. Torti *et al.* demonstrated choriocapillaris imaging by AO-OCT [74]. However, the imaging was only performed with intensity OCT and not with Doppler OCT.

In our result, intensity OCT showed only limited contrast. Alternatively, the Doppler power images showed capillary patterns. The reasons of the limited contrast in the intensity images can be explained by the scattering properties of tissues. According to the histology, the inter-capillary region contains collagen fibers [16]. Except the special case of cornea, collagenous tissue, such as sclera and lamina cribrosa, appeared with hyper-scattering in the OCT intensity image. Since the capillary is also hyper-scattering, this scattering property of the inter-capillary region would degrade the contrast of the choriocapillaris in the intensity images.

5. Conclusion

To the best of our knowledge, we are the first to demonstrate the AO-OCA by combining the AO-OCT and Doppler OCT. This enables the detailed investigation of a three-dimensional capillary network in the retina and choroid. The intensity and Doppler images showed similar contrast for the retinal capillaries. On the other hand, the choriocapillaris, pre-arterioles and post-venules in the Sattler layer were more highly contrasted by the Doppler technique. The AO-OCA is found to be useful especially in the detection of the choriocapillaris and choroidal capillary network without any contrast agent.